Eur. Phys. J. Appl. Phys. **35**, 201–210 (2006)
DOI: 10.1051/epjap:2006089

THE EUROPEAN PHYSICAL JOURNAL
APPLIED PHYSICS

# The effect of interionic distance on the properties of Al-doped Mn-Zn ferrites

M.A. Amer[1,a], S.A. Saafan[1], and S.M. Attia[2]

[1] Physics Department, Faculty of Science, Tanta University, Tanta, Egypt
[2] Phys. & Chem. Department, Faculty of Education, Kafer El-Shiekh, Egypt

Received: 2 May 2005 / Received in final form: 13 June 2006 / Accepted: 20 June 2006
Published online: 23 August 2006 – 

**Abstract.** Room temperature Mössbauer, X-ray and IR spectral studies were carried out for the spinel system $Mn_{0.5}Zn_{0.5}Al_xFe_{2-x}O_4$, $0 \leq x \leq 1$, prepared using the usual ceramic technique. X-ray patterns confirm that all samples have single phase cubic spinel structure. The Mössbauer spectra of the samples show a six-line magnetic pattern and a central paramagnetic phase. They are assigned to two magnetic subpatterns and two quadrupole doublets due to $Fe^{3+}$ ions at the tetrahedral A-sites and octahedral B-sites. The effect of increasing the $Al^{3+}$ content $x$ on the hyperfine interaction parameters is studied and discussed. The lattice constant, oxygen positional parameter, mean ionic radius of the A- and B-sites, bond lengths, edges and interionic distance are affected by the additional process $x$. They are determined and discussed as functions of $x$. The IR spectra shows six absorption bands in the range 222–1033 $cm^{-1}$. The bands are attributed to the corresponding metal-oxygen complexes in the A- and B-sites. The hyperfine interaction parameters, the IR band positions and intensities reveal their dependence on the $Fe^{3+}$–$O^{2-}$ bond length and the interionic distance at A- and B-sites. The variation of the quadrupole doublet splitting for the B-site and the oxygen parameter reveal the increasing trigonal distortion of the B-site oxygen coordination. The IR absorption at 222 $cm^{-1}$, the velocity of the infrared waves when passed through the samples and the jump rate of the lattice vacancies were found to decrease.

**PACS.** 78.30.-j Infrared and Raman spectra – 76.80.+y Mossbauer effect; other gamma-ray spectroscopy – 75.50.Gg Ferrimagnetics

## 1 Introduction

The spinel ferrites are ferrimagnetic semiconducting materials having a vast field of technological applications from microwave to radio frequencies. Their interesting structural, electrical and magnetic properties are affecting by the substitution of ions of different charges and radii, the preparation conditions and the ionic distribution amongst the tetrahedral site (A-site) and octahedral site (B-site). Intensive studies to determine the spinel ferrite properties have been carried out using Mössbauer, IR, X-ray and other techniques. Some authors studied the properties of ferrite systems containing $Zn^{2+}$ [1,2], $Zn^{2+}$ and $Mn^{2+}$ [3,4], and $Al^{3+}$ [5–7]. The obtained results revealed very interesting cation distribution, magnetic, structural and electric properties. It is well known that in spinel ferrites the $Zn^{2+}$ ions exclusively occupy A-sites [1,2], the $Mn^{2+}$ ions preferentially occupy B-sites [3,4], and $Al^{3+}$ ions occupy B-sites [5–7]. The existence of $Zn^{2+}$ ions on A-sites and $Al^{3+}$ ions on B-sites reduces the samples magnetization and affects the magnetic properties of the samples. Consequently, the purpose of this work is to study the effect of substituting $Al^{3+}$ ions instead of the magnetic $Fe^{3+}$ ions at B-sites on the hyperfine interaction and structural parameters of the spinel system $Mn_{0.5}Zn_{0.5}Al_xFe_{2-x}O_4$. The techniques used in this study are X-ray, Mössbauer and infrared spectrometry.

## 2 Experimental

The ferrite samples $Mn_{0.5}Zn_{0.5}Al_xFe_{2-x}O_4$ ($x$ = 0, 0.2, 0.4, 0.6, 0.8 and 1) were prepared by the high temperature solid-state reaction method. Powder mixtures of the appropriate proportions of the high purity starting materials (i.e. $MnCO_3$, ZnO, $Fe_2O_3$ and $Al_2O_3$) were heated for 20 hours at 1000 °C and cooled slowly. The samples were ground, pressed into pellets and heated at 1000 °C for 20 h and cooled slowly. Finally, the resulting samples were reground, repelletized and sintered for 20 h at 1250 °C in air then cooled slowly. The cooling process was carried out

[a] e-mail: moazamer@yahoo.com

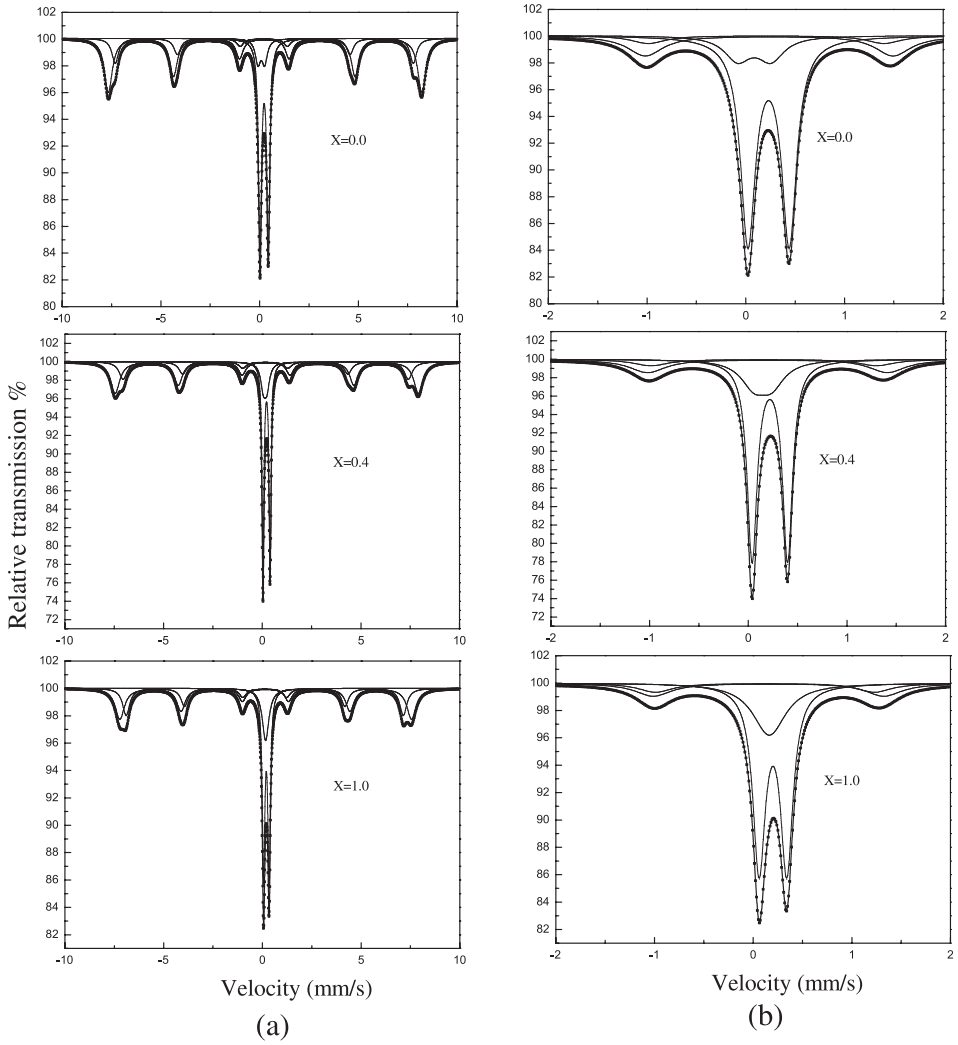


**Fig. 1.** (a) Some of the similar Mössbauer spectra of the $Mn_{0.5}Zn_{0.5}Al_xFe_{2-x}O_4$ ferrites taken at room temperature for $x = 0$, 0.4 and 1, and (b) their corresponding central paramagnetic phase.

in steps of 50 °C/20 minutes in the range 1250–800 °C, 100 °C/hour in the range 800–500 °C, then the samples left to cool gradually in the furnace to room temperature. The samples were ground to very fine powder to be used in the spectral analysis (The average size of the particles are estimated using the Scherer equation to be 21.3 nm).

The X-ray diffraction patterns were taken using a Shimazu X-ray diffractometer XD-3, and a $CuK_\alpha$ radiation source with wavelength $\lambda_o = 1.5418$ Å. The X-ray diffraction patterns confirmed the cubic spinel structure of the studied samples. The lattice constant, $a$, was determined for each reflection plane using the relation; $a = d_{hkl}\ (h^2 + k^2 + l^2)^{1/2}$, and the interplanar distance, $d_{hkl}$, was calculated using Bragg's equation.

The infrared patterns were recorded using a computerized Perkin-Elmer1430 infrared spectrometer and KBr pellets in the range 200 to 1100 $cm^{-1}$.

The Mössbauer spectra were recorded at room temperature using a $^{57}Co$ source in a rhodium matrix, and metallic iron was used for calibration. The spectra were analyzed by means of a least-squares fitting technique. The obtained spectra were similar and showed a six-line Zeeman pattern and a central paramagnetic phase C, as shown in Figure 1. The Mössbauer spectra were analyzed by means of a least-squares fitting computer program. The analysis of the six-line Zeeman pattern shows a good fit to two magnetic patterns due to $Fe^{3+}$ ions in A-sites (A) and $Fe^{3+}$ and $Fe^{2+}$ ions in B-sites (B). The paramagnetic phase, C, shows two quadrupole doublets due to $Fe^{3+}$ on A-sites ($C_A$) and on B-sites ($C_B$).

## 3 Results and discussions

### 3.1 Mössbauer spectra

Figure 1 shows some of the spectra taken for the samples with $x = 0.0$, 0.4, and 1 (a), and their central paramagnetic phase C (b). The existence of the paramagnetic phase C in the Mössbauer spectra may be due to the fact that a fraction of the B-site Fe ions have a few nearest

**Table 1.** Mössbauer parameters of the system $Mn_{0.5}Zn_{0.5}Al_xFe_{2-x}O_4$, where *IS*, *QS*, $\Gamma_{1,6}$ and $A_0$, are the isomer shift, the quadrupole shift, the outermost line width, and the fractional area of the corresponding pattern, respectively.

| $x$ | Subpattern | *IS* (mm/s) | *QS* (mm/s) | $\Gamma_{1,6}$ (mm/s) | $A_0$ |
|---|---|---|---|---|---|
| 0 | A | 0.22 | 0.03 | 0.4 | 0.17 |
| | B | 0.26 | 0.04 | 0.49 | 0.45 |
| | $C_A$ | 0.1 | 0.34 | 0.32 | 0.07 |
| | $C_B$ | 0.23 | 0.42 | 0.57 | 0.31 |
| 0.2 | A | 0.19 | 0.01 | 0.37 | 0.19 |
| | B | 0.23 | 0.03 | 0.56 | 0.44 |
| | $C_A$ | 0.13 | 0.21 | 0.3 | 0.07 |
| | $C_B$ | 0.22 | 0.4 | 0.42 | 0.3 |
| 0.4 | A | 0.17 | 0.02 | 0.48 | 0.2 |
| | B | 0.21 | 0.04 | 0.56 | 0.42 |
| | $C_A$ | 0.15 | 0.18 | 0.31 | 0.09 |
| | $C_B$ | 0.22 | 0.36 | 0.38 | 0.29 |
| 0.6 | A | 0.14 | 0.02 | 0.45 | 0.21 |
| | B | 0.19 | 0.03 | 0.53 | 0.41 |
| | $C_A$ | 0.16 | 0.11 | 0.29 | 0.1 |
| | $C_B$ | 0.2 | 0.34 | 0.42 | 0.28 |
| 0.8 | A | 0.12 | 0.02 | 0.42 | 0.22 |
| | B | 0.18 | 0.03 | 0.51 | 0.38 |
| | $C_A$ | 0.16 | 0.06 | 0.28 | 0.11 |
| | $C_B$ | 0.22 | 0.3 | 0.38 | 0.29 |
| 1 | A | 0.12 | 0.0 | 0.43 | 0.24 |
| | B | 0.16 | 0.01 | 0.56 | 0.36 |
| | $C_A$ | 0.16 | 0.0 | 0.41 | 0.11 |
| | $C_B$ | 0.2 | 0.28 | 0.37 | 0.29 |
| error | | ±0.02 | ±0.02 | ±0.02 | ±0.01 |

A-site magnetic neighbours having ordered spins and giving rise to the quadruple doublet [8]. The existence of the six-line magnetic pattern is due to the superexchange interaction between the magnetic ions on the A- and B-sublattices [9]. Statistical fluctuations in the distribution of the magnetic and non–magnetic ions are believed to be responsible for this behaviour [10]. The existence of the quadrupole doublet $C_A$ in the spectra could be attributed to randomisation of cations with different charges and radii at A- and B-sites [11]. The Mössbauer parameters are listed in Table 1.

The results show that the $Fe^{3+}$ isomer shift values *IS* of A-sites ($IS_A$) and B-sites ($IS_B$) lie between 0.1 and 0.26 mm/s, which are characteristic of the pure $Fe^{3+}$ ions [12,13]. Both $IS_A$ and$IS_B$ decrease with increasing $Al^{3+}$ ions content. This behavior indicates that the local crystal chemistry and *s*-electron charge distribution of $Fe^{3+}$ ions are affected by $Al^{3+}$ substitution. The decrease of $IS_A$ and $IS_B$ with increasing $Al^{3+}$ content could be attributed to the changes of $Fe^{3+}$–$O^{2-}$ bond length at the A- and B-sites [14,15]. The quadrupole shift values *QS* of the A and B magnetic patterns (Tab. 1) are very small. This indicates that the local symmetry of the magnetic phase of the A-sites is close to cubic $T_d$ while that of B-sites is close to trigonal. These *QS* values of the magnetic patterns A and B are consistent with that reported previously [8].

Figure 2a shows the compositional dependence of the hyperfine magnetic field of A-sites, $H_A$, and B-sites, $H_B$. The results show that $H_B$ is always greater than $H_A$ and both $H_A$ and $H_B$ decrease with increasing $x$. This can be explained on the basis of the covalent character of the bond $Fe^{3+}$–$O^{2-}$ and changes in its length at A- and B-sites. The bond $Fe^{3+}$–$O^{2-}$ is more covalent at the A- site than that at the B-site, whereas the *s*-electron charge density at the A-site $Fe^{3+}$ nucleus is larger [14,15]. This results in higher values of $H_B$ and $IS_B$ than $H_A$ and $IS_A$, respectively. The decrease of $H_A$ and $H_B$ with $x$ may be due to the reduction of the number of magnetic bonds $Fe_A^{3+}$–$O^{2-}$–$Fe_B^{3+}$ by replacement of $Fe^{3+}$ ions by nonmagnetic $Al^{3+}$ ions. This leads to a reduction of A–B superexchange interaction which in turn leads to a decrease of both $H_A$ and $H_B$. Consequently, the reduction of $Fe^{3+}$ ions results in a decrease of the magnetization. In ferrites, the spontaneous magnetization *Ms* of the bulk material can be obtained as explained early [3,8,16]. The hyperfine field of the corresponding pattern has been multiplied by its fractional area, and the difference, $Ms = M_B$–$M_A$,

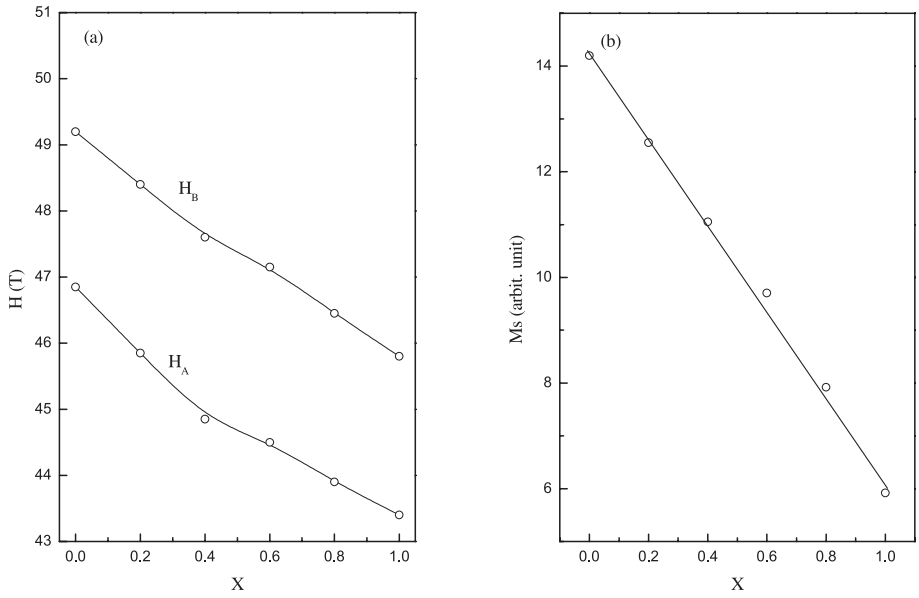


**Fig. 2.** Compositional dependence of the hyperfine magnetic field of the A- and B-sites, $H_A$ and $H_B$ (a), and the bulk magnetization $Ms$ (b).

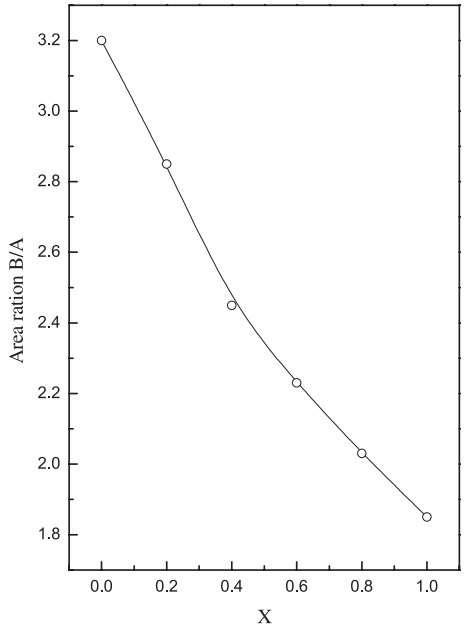


**Fig. 3.** Variation of the area ratio B/A with $x$.

gives a measure of the spontaneous magnetization of the bulk material. Figure 2b illustrates that $Ms$ decreases with $x$, which can be explained by the decrease of the magnetic fields $H_A$ and $H_B$ with $x$ [16].

The distribution of $Fe^{3+}$ ions amongst A- and B-sites could be obtained by calculating the ratio of the areas of the resolved subspectra for B- and A-sites. Figure 3 shows the compositional dependence of the area ratio B/A. It is shown that the area ratio B/A decreases with $x$, which indicates that the $Al^{3+}$ concentration is increased at the expense of the $Fe^{3+}$ ions at B-sites. The cation distribution of the samples (Tab. 2) can be estimated using both

**Table 2.** The cation distribution of the spinel system $Mn_{0.5}Zn_{0.5}Al_xFe_{2-x}O_4$.

| $x$ | A-sites | B-sites |
|---|---|---|
| 0 | $Zn_{0.5}Mn_{0.02}Fe_{0.48}$ | $Mn_{0.48}Fe_{1.52}$ |
| 0.2 | $Zn_{0.5}Mn_{0.03}Fe_{0.47}$ | $Mn_{0.47}Fe_{1.33}Al_{0.2}$ |
| 0.4 | $Zn_{0.5}Mn_{0.04}Fe0_{.46}$ | $Mn_{0.46}Fe_{1.14}Al_{0.4}$ |
| 0.6 | $Zn_{0.5}Mn_{0.07}Fe_{0.43}$ | $Mn_{0.43}Fe_{0.97}Al_{0.6}$ |
| 0.8 | $Zn_{0.5}Mn_{0.1}Fe_{0.4}$ | $Mn_{0.4}Fe_{0.8}Al_{0.8}$ |
| 1 | $Zn_{0.5}Mn_{0.15}Fe_{0.35}$ | $Mn_{0.35}Fe_{0.65}Al_1$ |

the area ratio of the A- and B-subspectra and the well-known site preference of cations [1–7]. It is known that the $Zn^{2+}$ ions exclusively occupy A-site [1,2] and $Al^{3+}$ ions the B-sites [5–7]. The $Mn^{2+}$ ions preferentially occupy B-sites [3,4], and under some circumstances they can migrate into the A-site leading to inverse spinel ferrites.

The outermost line width $\Gamma_{1,6}$ of the A and B magnetic patterns, $\Gamma_A$ and $\Gamma_B$, lie between 0.37 and 0.56 mm/s (Tab. 1). It is clear that $\Gamma_B$ is broader than $\Gamma_A$, which may be due to the random distribution of the Zn, Mn and/or $Fe^{3+}$ ions amongst the A-sites as nearest neighbours of the B-site $Fe^{3+}$ ions.

The quadrupole doublet splitting of $C_A$ ($QS_A$) and $C_B$ ($QS_B$) was determined for each sample and listed in Table 1. Both $QS_A$ and $QS_B$ decrease with $x$ and the values of $QS_A$ are less than those of $QS_B$. The decrease of $QS$ values may be ascribed to the change of $Fe_A^{3+}$–$O^{2-}$bond length [14,15]. The relation between $QS$ values and the oxygen positional parameter $u$ (Sect. 3.2) is shown in Figure 4. This behavior shows a negative correlation of $QS_A$ and $QS_B$ versus $u$, which confirms the effect of the bond length on the $QS$ values [10,17,18]. The decrease of $QS_A$ and $QS_B$ with $x$ may be due to the decrease of $Fe^{3+}$ content in these interstices as proposed by Evans et al. [19].

**Table 3.** The lattice parameter $a_t$, the bond length of the A-sites $d_{AL}$ and of the B-sites $d_{BL}$, the tetrahedral edge $d_{AE}$, the shared and unshared octahedral edges, $d_{BE}$ and $d_{BEU}$, and the hopping length at the A- and B-site, $L_A$ and $L_B$, respectively.

| $x$ | $a_t$ (Å) | $d_{AO}$ (Å) | $d_{BO}$ (Å) | $d_{AE}$ (Å) | $d_{BE}$ (Å) | $d_{BEU}$ (Å) | $L_A$ (Å) | $L_B$ (Å) |
|---|---|---|---|---|---|---|---|---|
| 0.0 | 8.456 | 2.188 | 1.93 | 3.545 | 2.435 | 1.075 | 3.662 | 2.99 |
| 0.2 | 8.45 | 2.189 | 1.927 | 3.546 | 2.428 | 1.075 | 3.659 | 2.987 |
| 0.4 | 8.406 | 2.191 | 1.914 | 3.552 | 2.397 | 1.071 | 3.64 | 2.972 |
| 0.6 | 8.363 | 2.196 | 1.895 | 3.572 | 2.342 | 1.068 | 3.621 | 2.957 |
| 0.8 | 8.301 | 2.2 | 1.872 | 3.585 | 2.285 | 1.063 | 3.594 | 2.935 |
| 1 | 8.245 | 2.205 | 1.851 | 3.591 | 2.239 | 1.058 | 3.57 | 2.915 |

Error = ±0.005

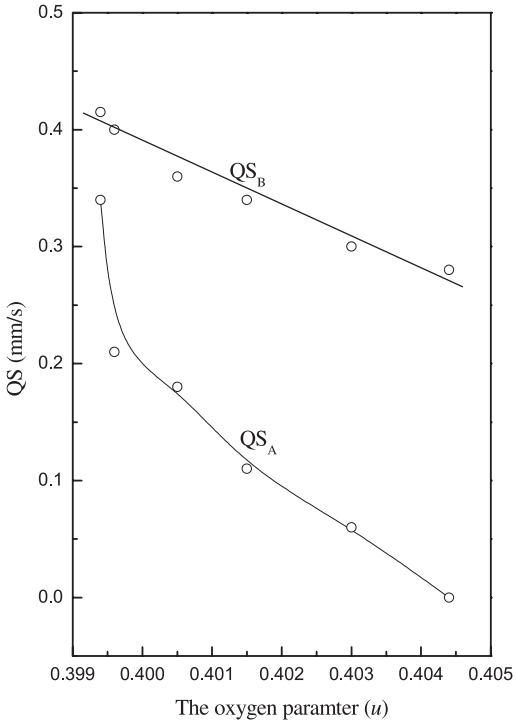


**Fig. 4.** The quadrupole doublet splitting $QS$ at A- and B-sites versus the oxygen positional parameter $u$.

They indicated that an important contribution of the electric field gradient EFG arises from the $d$–electron of the $Fe^{3+}$–$O^{2-}$ bond, where a decrease of $Fe^{3+}$ ions leads to decreasing EFG. Table 1 confirms that the fractional area of the paramagnetic phase is independent of the $Al^{3+}$ concentration $x$.

### 3.2 X-ray analysis

The values of the lattice constant, $a_t$, were determined using the extrapolating function [5]. These values lie between 8.456 and 8.245 Å as listed in Table 3. It is illustrated that the values of $a_t$ decrease with increasing $Al^{3+}$ ion content. This behaviour may be attributed to the change of the ionic radii of the cations, where the ionic radius of $Al^{3+}$ ion (0.57 Å) is smaller than that of $Fe^{3+}$ ion (0.67 Å). These results agree with that obtained previously in studying the Mn–Zn ferrites [3], and Al-doped ferrites [5,7,16].

The mean ionic radius of A-site ($R_A$) and B-site ($R_B$) for each sample were calculated from the relations [20,21];

$$R_A = \frac{1}{2} r_{\text{tet.Zn}^{2+}} + \left(\frac{1}{2} - y\right) r_{\text{tet.Fe}^{3+}} + y r_{\text{tet.Mn}^{2+}}$$

$$R_B = \left(\frac{1}{2} - y\right) r_{\text{oct.Mn}^{2+}} + x r_{\text{oct.Al}^{3+}} + (1.5 + y - x) r_{\text{oct.Fe}^{3+}}$$

where $y$ is the $Mn^{2+}$concentration in A-sites. Using the values of the oxygen ionic radius $r_o$, $a_t$ and $R_A$, the oxygen positional parameter $u$ was deduced from the relation [21];

$$R_A = a_t\sqrt{3}(u - 0.25) - r_o.$$

The obtained values of $u$, $R_A$ and $R_B$ are plotted versus $x$ in Figure 5b. It is clear that the obtained values of $u$ are higher than the standard value 0.375, and agree with those obtained for Al-ferrites [10,16]. Figure 5b shows that $R_A$ and $u$ increase linearly with $x$, whereas $R_B$ decreases linearly. The increase of $R_A$ may be due to the migration of the larger $Mn^{2+}$ ions (0.82 Å) instead of $Fe^{3+}$ ions at the A-sites (Tab. 2). The decrease of $R_B$ may be due to the replacement of $Fe^{3+}$ ions by the smaller $Al^{3+}$ at B-sites [7]. The increasing migration of the larger $Mn^{2+}$ ions to A-sites leads to a progressive expansion of the A-site interstices in order to accommodate these $Mn^2$ ions [16,22]. This expansion makes the anions move away from the nearest A-site cations in the [111] direction, hence increasing the tetrahedron size without changing its symmetry, which in turn leads to increasing $R_A$ and the A-site bond length $d_{AO}$. This displacement of the anions leads to increasing the oxygen parameter $u$ with $x$.

The interionic distances, i.e. cation–anion distances amongst the A- and B-sites, $d_{AO}(d_{\text{Fe}_A^{3+}-\text{O}^{2-}})$ and $d_{BO}(d_{\text{Fe}_B^{3+}-\text{O}^{2-}})$, together with the distance of closest anion–anion approach, i.e. the tetrahedral edge $d_{AE}$ and the shared and unshared octahedral edges, $d_{BE}$ and $d_{BEU}$,

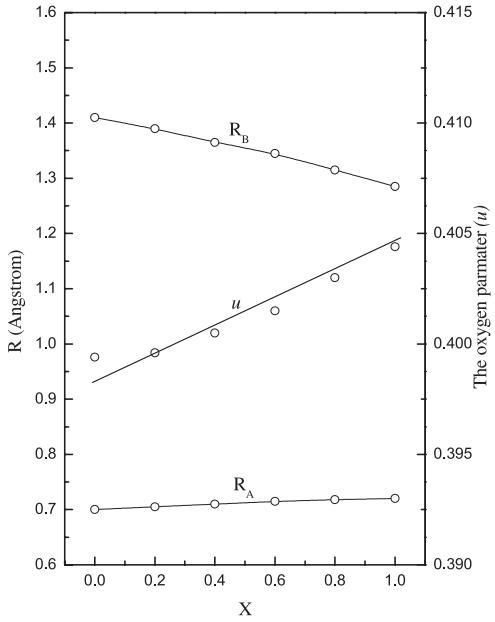


**Fig. 5.** The ionic radius of the A-site, $R_A$, and B-site, $R_B$, and the oxygen positional parameter $u$ as functions of the $Al^{3+}$ content $x$.

respectively, can be calculated using the equations [23];

$$d_{AO} = a_t\sqrt{3}\ (u - 0.25)$$
$$d_{BO} = a_t\left(3u^2 - \frac{11}{4}u + \frac{43}{64}\right)^{1/2}$$
$$d_{AE} = a_t\sqrt{2}\,(2u - 0.5)$$
$$d_{BE} = a_t\sqrt{2}\,(1 - 2u)$$
$$d_{BEU} = a_t\left(4u^2 - 3u + \frac{11}{16}\right)^{1/2}.$$

The obtained values are given in Table 3. It is clear that the values of $d_{AO}$ and $d_{AE}$ increase slowly while that of $d_{BO}$, $d_{BE}$ and $d_{BEU}$ decrease as functions of the $Al^{3+}$ ion concentration $x$. This variation may be attributed to the substitution process and the cation distribution (Tab. 2). The increase of $d_{AO}$ and $d_{AE}$ may be due to the enlargement of A-site interstices resulting from the cation distribution. Arean et al. [23] explained a mechanism by which the tetrahedral interstices are enlarged because A-site interstices are very sensitive to small displacements of the anions. The anions move away from the nearest A-site cation in the [111] direction causing the increase of the A-site size relative to the ideal close-packed anion arrangement but without changing its $T_d$ symmetry. The B-site interstices are less sensitive to small changes of $u$, however the displacement of anions which enlarges $u$ above 0.375, causes a distortion of the B-site symmetry. This distortion, in addition to the expansion of the A-site interstices, leads to a shortening of the B-site shared edge $d_{BE}$ and the unshared edge $d_{BEU}$ bringing the anions into close contact along those edges [18,23].

The distance $L_A$ between the magnetic ions $Fe^{3+}$ and $Mn^{2+}$ at the A-site can be obtained from the equation

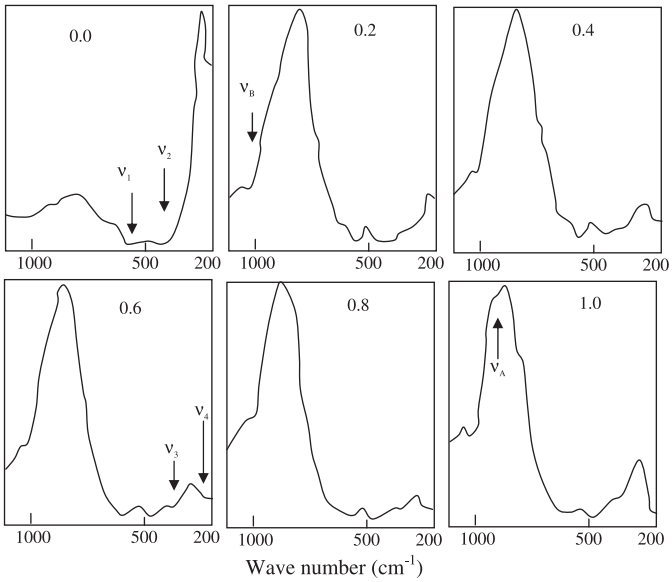


**Fig. 6.** The recorded infrared spectra of the ferrites $Mn_{0.5}Zn_{0.5}Al_xFe_{2-x}O_4$.

$L_A = a_t\sqrt{3}/4$, and at the B-site from $L_B = a_t\sqrt{2}/4$ [24]. The resultant values are given in Table 3. It is clear that $L_A$ and $L_B$ reflect the same behavior of $a_t$, where they decrease with increasing $Al^{3+}$ concentration, $x$, in the samples. This may be due to the reduction of the unit cell arising from the substitution process and the migration of the magnetic $Mn^{2+}$ ions into A-interstices, causing the magnetic ions to approach each other at these sites.

### 3.3 Infrared spectra

Figure 6 shows the IR spectra for all samples studied, where the absorption band positions and intensities are listed in Table 4. The band $\nu_1$ was assigned to $Fe^{3+}$–$O^{2-}$ bonds at the A-site and $\nu_2$ to $Fe^{3+}$–$O^{2-}$ and $Al^{3+}$–$O^{2-}$ bonds at the B-site. The shoulder that appears in the band $\nu_1$ was assigned to $Zn^{2+}$–$O^{2-}$ bonds at the A-sites. However, the growth of that shoulder may be due to the increase of the number of $Mn^{2+}$–$O^{2-}$ bonds at A-sites [4], which support the deduced cation distribution (Tab. 2). The band $\nu_3$ was observed in the range 344–420 $cm^{-1}$ and assigned to $Mn^{2+}$–$O^{2-}$ bond at the B-site. The band $\nu_4$ was observed at the position 222 $cm^{-1}$ and assigned to some type of lattice vibrations [3–5,25,26]. Earlier, the bands $\nu_1$, $\nu_2$, $\nu_3$ and $\nu_4$ were observed in the IR spectra recorded for the spinel ferrites [3–5,10,25,26] in the range 200–640 $cm^{-1}$.

The position of the absorption bands $\nu_1$ and $\nu_2$ show a shift towards higher energy after $Al^{3+}$ substitution instead of $Fe^{3+}$ ions. This may be explained on the basis of a decrease in the concentration of $Fe^{3+}$ ions amongst A- and B-sites, which leads to an increase in the metal-oxygen stretching vibrational energies and reduces the size of the unit cell $a_t$ [3]. Table 4 indicates that the band intensities; $I_2$ and $I_3$ are compositional independent, whereas $I_4$ decreases and the trend of $I_1$ increases with $x$. The variation

**Table 4.** The infrared absorption bands $\nu_n$, $n = 1$, 2, 3 and B, where $\nu_A$ appears only in the spectrum for $x = 1$, at 923 cm$^{-1}$. Sh denotes a shoulder of the spectrum.

| $x$ | $\nu_1$ (cm$^{-1}$) | $I_1$ | $\nu_2$ (cm$^{-1}$) | $I_2$ | $\nu_3$ (cm$^{-1}$) | $I_3$ | $\nu_4$ (cm$^{-1}$) | $I_4$ | $\nu_B$ (cm$^{-1}$) | $I_B$ |
|---|---|---|---|---|---|---|---|---|---|---|
| 0.0 | 550 | 3.2 | 437 | 3.7 | sh | | 222 | 41.3 | 1054 | 14 |
| 0.2 | 562 | 3.4 | 436 | 3.2 | 344 | 4 | 222 | 11.5 | 1029 | 26 |
| 0.4 | 579 | 4.1 | 446 | 4.2 | 354 | 4.2 | 222 | 7 | sh | |
| 0.6 | 582 | 3.4 | 455 | 3.3 | 420 | 4.1 | 222 | 4.1 | sh | |
| 0.8 | 584 | 3.8 | 464 | 3.2 | 399 | 4.5 | 222 | 3.5 | 1033 | 30 |
| 1 | 586 | 4.6 | 466 | 4.1 | sh | | 222 | 2.6 | 1026 | 35 |
| Error | ±1 | ±0.2 | ±1 | ±0.2 | ±1 | ±0.2 | ±1 | ±0.2 | ±1 | ±0.2 |

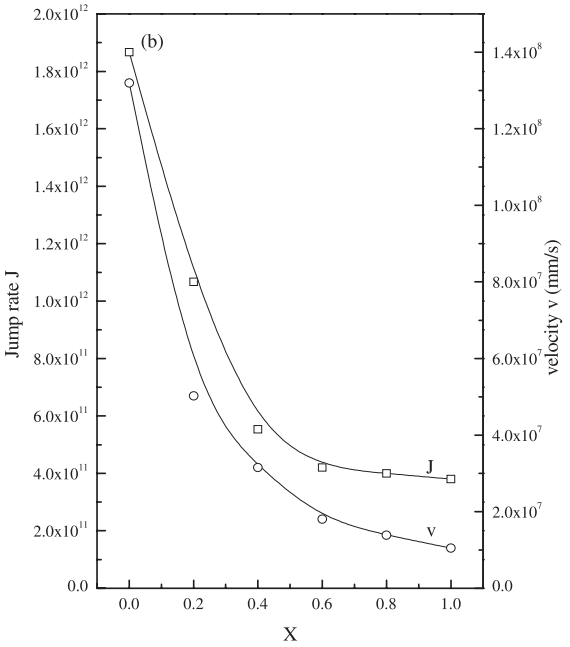


**Fig. 7.** Effect of $Al^{3+}$ content on IR velocity $V$ and the jump rate $J$ of lattice vacancies.

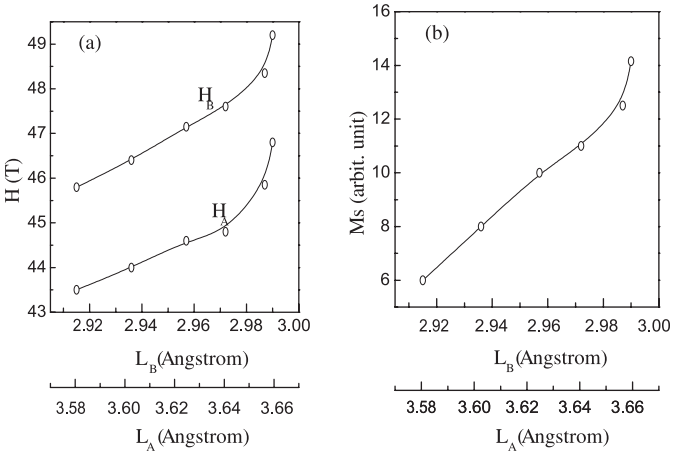


**Fig. 8.** Effect of the distance between the magnetic ions at the A-sites, $L_A$, and B-sites, $L_B$, on (a) the hyperfine magnetic fields $H_A$ and $H_B$, and (b) the magnetization $Ms$.

of $I_1$ and $I_4$ is due to the change of the $Fe^{3+}$–$O^{2-}$ bond length. The trend of $I_1$ increasing may be due to increasing $d_{AO}$ and the decrease of $I_4$ may be due to decreasing the divalent metal-oxygen bond length at A-sites with $x$.

Figure 6 and Table 4 show two new absorption bands; $\nu_A$ lies at 923 cm$^{-1}$ and $\nu_B$ lies between 1026 and 1054 cm$^{-1}$. The band $\nu_A$ appeared only for the sample with $x = 1$ but the shoulder and broadness of the spectra illustrate its presence for all samples.

The bands $\nu_A$ and $\nu_B$ become pronounced with increasing $x$. These bands have been seen previously in studying spinel ferrites [27–29]. The band $\nu_A$ was attributed to the breaking mode of the A-site or to a compound due to distribution of particle morphologies. The band $\nu_B$ may be assigned to the highest frequency mode of lattice vibrations or to increasing the trigonal distortion of the B-site oxygen coordination i.e. increasing the oxygen positional parameter $u$ [10]. The bands $\nu_A$ and $\nu_B$ have been observed in studying Ni-Zn ferrites [28], and assigned to the presence of $Fe^{2+}$ in both A- and B-sites.

The jump rate $J$ of the lattice vacancies may be estimated from the relation [25,30–33]: $J = \nu e^{E/kT}$, where $\nu$ is the frequency of the vibration, $k$ is the Boltzmann constant, $E = h\nu = hV/\lambda$, $h$ is the Planck's constant and $\lambda$ is the IR wavelength. Figure 7 illustrates that the IR velocity $V$ and jump rate $J$ of the lattice vacancies decreases with increasing $Al^{3+}$ concentration $x$. The substitution of $Al^{3+}$ instead of $Fe^{3+}$ ions at the B-interstices dilutes the B–B magnetic interactions and decreases the $Fe^{3+}$–$O^{2-}$ bond length at these interstices (Tab. 4). This causes the lattice to vibrate at low frequencies with the incident IR waves and decreases the IR wave velocity $V$ inside the samples [25]. The decrease of the jump rate $J$ is attributed to increasing $Al^{3+}$ content and decreasing cation vacancies. The smaller $Al^{3+}$ ions fill some of the lattice vacancies created by replacing $Fe^{3+}$ ions and migrating $Mn^{2+}$ ions into the A-sites, causing the decrease of the cation vacancies at these sites and the decrease of the jump rate [25,33].

### 3.4 The effect of the interionic distances

The dependence of the hyperfine magnetic fields $H_A$ and $H_B$ and magnetization $Ms$ on the distance between the magnetic ions $L_A$ and $L_B$ is shown in Figure 8. It is shown that the lowest values of $H_A$, $H_B$ and $Ms$ correspond to

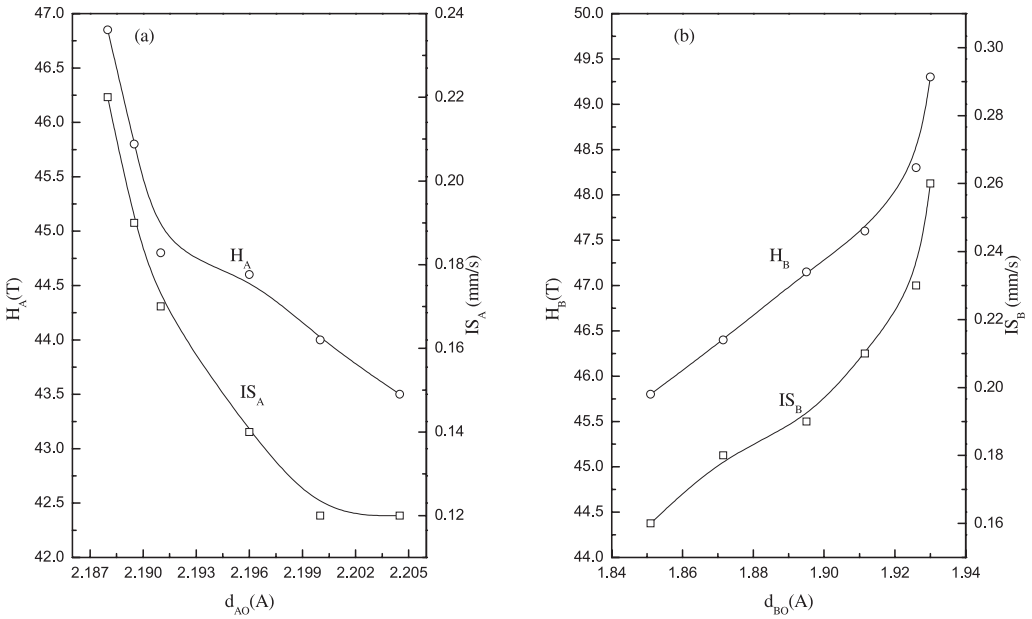


**Fig. 9.** Dependence of (a) the A-site magnetic field $H_A$ and isomer shift $IS_A$ on the bond length $d_{AO}$, and (b) the B-site magnetic field $H_B$ and isomer shift $IS_B$ on the bond length $d_{BO}$.

$x = 1$, i.e. the least A–A and B–B ionic distance. This confirms that the A–B magnetic exchange interaction exceeds the A–A and B–B antiferromagnetic direct interactions in these samples. The increase of $H_A$, $H_B$ and $Ms$ versus $L_A$ and $L_B$ can be explained as follows; (1) the increase of $L_A$ and $L_B$ leads to increase of the cation–cation overlap and the $s$-electron density, which is reflected in increasing $H_A$, $H_B$ and $Ms$. (2) Increasing $L_A$ and $L_B$ forces some of the $Fe^{3+}$ ions to enter the A-sublattices, as a result $H_A$, $H_B$ and $Ms$ increase. (3) The existence of high concentration ($x = 1$) of the smaller size diamagnetic $Al^{3+}$ ions amongst the B-sites reduces the distance between the magnetic ions and dilutes the magnetic interactions between them. The increase of $L_A$ and $L_B$, due to increasing the content of $Fe^{3+}$ at the expense of $Al^{3+}$ ions, leads to increasing the magnetic interactions between the magnetic ions.

The correlation between both $H_A$ and $IS_A$ and the bond $Fe_A^{3+}$–$O^{2-}$ length $d_{AO}$ and between both $H_B$ and $IS_B$ and the bond $Fe_B^{3+}$–$O^{2-}$ length $d_{BO}$ is illustrated in Figure 9 respectively. It is illustrated that $H_A$ and $IS_A$ decrease with $d_{AO}$, whereas $H_B$ and $IS_B$ increase with $d_{BO}$. The increase of $H_B$ and $IS_B$ may be explained as follows The increase of the bond length $d_{BO}$ causes a decrease of the $d$–electron covalent character of the bond $Fe_B^{3+}$–$O^{2-}$, which in turn causes a decrease of the $s$–$d$ orbital overlap and hence, $H_B$ and $IS_B$ increase with $d_{BO}$ [14,15,34]. The decrease of $H_A$ and $IS_A$ may be due to increase of the oxygen vacancies (i.e. increasing $u$) in A-sites arising from the expansion of their interstices (Sect. 3.2). These vacancies cause the increase of the $s$–$d$ orbital overlap. As a result the $d$–electron covalent character of the bond $Fe_A^{3+}$–$O^{2-}$ increases and thus, $H_A$ and $IS_A$ decrease with $d_{AL}$ [35].

The variation of the band position $\nu_1$ against $d_{AO}$ and $\nu_2$ against $d_{BO}$ are plotted in Figure 10, respectively. Figure 10a indicates that $\nu_1$ increases nonlinearly with $d_{AO}$. It may be that increasing the length of bond $Fe_A^{3+}$–$O^{2-}$ depresses it, causing the increase in the resonant frequency of these groups [25]. The change of the $\nu_1$ increment rate for $d_{AO} > 2.191$ Å may be due to cluster formation in the samples, which distorts the $Fe_A^{3+}$–$O^{2-}$ bond length. The decrease of $\nu_2$ against $d_{BO}$ may be due to the increase of magnetic $Fe^{3+}$ and $Mn^{2+}$ ions at the B-sites. This will increase the B–B magnetic interactions at these sites, which suppresses the resonant frequency of these groups. On the other hand a decrease of the number of $Al^{3+}$–$O^{2-}$ bonds at B-sites will cause the band $\nu_2$ to appear at the highest resonant frequency of the B-site group because the nonmagnetic $Al^{3+}$ ion does not contribute to the B–B magnetic interactions.

Figures 9a and 10a show a change of the $H_A$ and $IS_A$ decrement rate and the $\nu_1$ increment rate with $d_{AO} > 2.191$ Å, respectively, and Figure 4b shows a change of $QS_A$ with $u \geq 0.4$. This may be due to cluster formation in the samples, which affects the $Fe_A^{3+}$–$O^{2-}$ bond length and $s$–$d$ orbital overlap [36].

## 4 Conclusion

The $Mn_{0.5}Zn_{0.5}Al_xFe_{2-x}O_4$ ferrites have been studied using Mössbauer, X-ray and IR spectroscopy. Analysis of the Mössbauer spectra shows two magnetic patterns, A and B, and two quadrupole doublets, $C_A$ and $C_B$, assigned to $Fe^{3+}$ ions at the A- and B-sites. The isomer and quadrupole shifts and the magnetic fields $H_A$ and $H_B$ of the magnetic patterns A and B, the bulk magnetization $Ms$ and the area ratio B/A of the B- to A-sites indicate dependence on the $Al^{3+}$ content $x$. The cation distribution has been estimated from the area under the

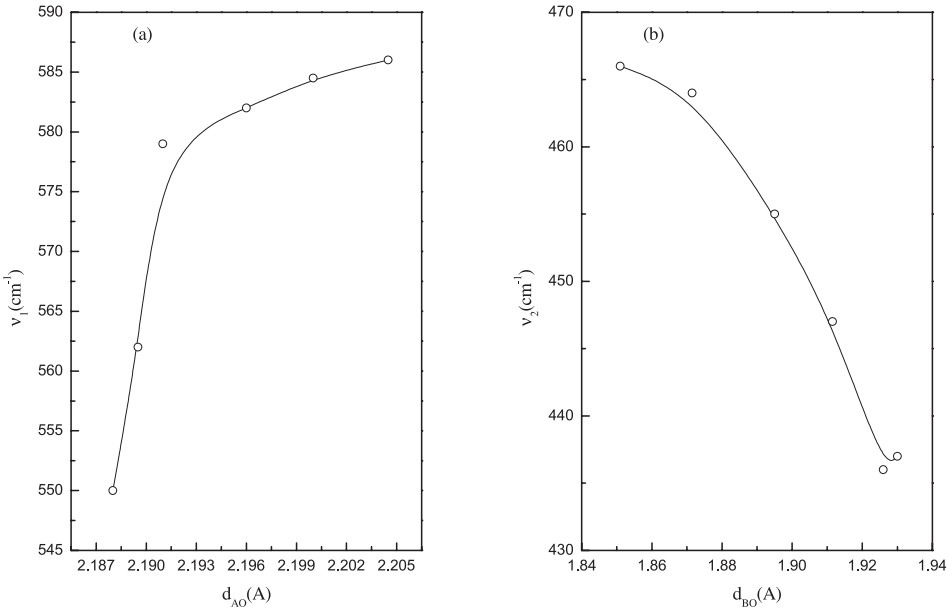


**Fig. 10.** Plot of (a) the tetrahedral band position $\nu_1$ versus $d_{AO}$, and (b) the octahedral band position $\nu_2$ versus $d_{BO}$.

well-resolved Mössbauer patterns and site preference of elements. The quadrupole doublet splittings $QS_A$ and $QS_B$ were affected by increasing $x$ and showed a negative correlation with the oxygen positional parameter $u$. The calculated X-ray parameters; the lattice parameter, $u$ and ionic radius, the bond length, edges and hopping length of the A- and B-sites were $x$-dependent. The increase of $u$ against $x$ indicated the increase of the B-site trigonal distortion with increasing $Al^{3+}$ ion content in the samples. Six absorption bands were observed in the infrared spectra in the range 222–1033 cm$^{-1}$. Each of these bands was assigned to a corresponding metal–oxygen bond, where the IR band positions and intensities were $x$-dependent.

Using the infrared band 222 cm$^{-1}$ ($4.505 \times 10^{-3}$ cm), it has been found that the IR velocity and the jump rate of the lattice vacancies decreases with increasing $x$. $H_A$, $H_B$, $IS_A$, $IS_B$, $QS_A$ and $QS_B$ and the band position and intensity of the A- and B-sites show a dependence on the Fe–O bond length, and $H_A$, $H_B$ and $Ms$ were also dependent on the distance between the magnetic ions at the A- and B-sites.

## References


1. D.H. An, K.U. Kang, B.G. Lee, J.B. Lim, S.U. Jang, K.S. Baek, E.J. Choi, H.N. Oak, Phys. Status Solidi B **241**, 383 (2003)
2. M. Siddique, M. Anwar-Ul-Islam, N.M. Butt, T. Abbas, Misbah-Ul-Islam, Phys. Status Solidi B **216**, 1069 (1999)
3. M.A. Amer, Phys. Status Solidi A **151**, 205 (1995)
4. O.M. Hemeda, J. Magn. Magn. Mater. **251**, 50 (2002)
5. O.M. Hemeda, M.A. Amer, S. Aboul-Enein, M.A. Ahmed, Phys. Status Solidi A **156**, 29 (1996)
6. S.S. Ata-Allah, M.K. Fayek, Phys. Status Solidi A **175**, 725 (1999)
7. A.M. Abo El Ata, S.M. Attia, T.M. Meaz, Solid State Sci. **6**, 61 (2004)
8. D.C. Dobson, J.W. Linnet, M.M. Rahman, J. Phys. Chem. Solids **31**, 727 (1970)
9. H.N. Ok, K.S. Baek, H.S. Lee, C.S. Kim, Phys. Rev. B **41**, 62 (1990)
10. M.A. Amer, Hyper. Interact. **131**, 29 (2000)
11. B.J. Evans, S.S. Hafner, J. Phys. Chem. Solids **29**, 1573 (1968)
12. G.K. Shenoy, F.E. Wagner, *Mössbauer Isomer shifts* (North-Holland Publ. Co., Amsterdam, 1978)
13. M.K. Fayek, F.M. Sayed Ahmed, S.S. Ata-Allah, M.K. Elnimr, M.F. Mostafa, J. Mater. Sci. **27**, 4813 (1992)
14. N.A. Halasa, G. De Pasquali, H.G. Drickamer, Phys. Rev. B **10**, 154 (1974)
15. V.I. Nikolaev, V.S. Rusakov, N.I. Chistyakova, Phys. Status Solidi A **91**, K139 (1982)
16. A.K.M. Zakaria, M.A. Asgar, S.G. Eriksson, F.U. Ahmed, S.M. Yunus, R.G. Delaphane, V. Stanciu, P. Svedlindh, Mater. Res. Bull. **39**, 1141 (2004)
17. De Grave, A. Covaeret, D. chambere, G. Robrecht, J. Phys. Coll. **C2**, 669 (1985)
18. R. Valeerberghe, R.E. Vandenberghe, Hyperline Interact. **23**, 75 (1985)
19. B.J. Evans, M.W. Ferguson, in *Proceedings of the International Conference of Magnetism ICM-**73** Nauka, Moscow, 1974*, Vol. 2, p. 249
20. P. Venugopal Reddy, T. Seshegirirao, J. Less-Common Metals **75**, 255 (1980)
21. O. Ravinder, J. Appl. Phys. **75**, 6121 (1994)
22. A.A. Yousif, M.E. Elzain, S.A. Mazen, S.S. Sutherland, M.H. Abdallah, S.F. Mansour, J. Phys.-Cond. Matter **6**, 5717 (1994)
23. C. Otero Arean, E. Garcia Diaz, J.M. Rubio Gonzalez, M.A. Villa Garcia, J. Sol. State Chem. **77**, 275 (1988)
24. M. El-Saadawy, M.M.M. Barakat, J. Magn. Magn. Mater. **213**, 309 (2000)
25. I.M. Hamada, J. Magn. Magn. Mater. **271**, 318 (2004)

26. M.H. Mahmoud, M.I. Abd-Elrahman, Atef M. Abdalla, A.I. Abdel-Mageed, Phys. Status Solidi **226**, 369 (2001)
27. V.A. Potakva, N.D. Zverev, V.P. Ramanov, Phys. Status Solidi A **12**, 623 (1972)
28. M.I. Baraton, V. Lorenezelli, G. Busca, R.J. Willey, J. Mater. Sci. Lett. **13**, 275 (1994)
29. M.K. El Nimr, M.A. Ahmed, M.A. El Hiti, J. Mater. Sci. Lett. **13**, 1500 (1994)
30. J. Neumann, M.O. Rowe, H. Veenhuis, R. Pankrath, E. Kratzig, Phys. Status Solidi B **215**, R9 (1999)
31. T. Tsurumi, T. Ichikawa, T. Harigai, H. Kakemoto, S. Wada, J. Appl. Phys. **91**, 2284 (2002)
32. U. Dorfler, R. Piechatzek, T. woike, M. Imlau, V. Wirth, L. Bohaty, T. Volk, R. Pankrath, M. Wohlecke, Appl. Phys. B **68**, 843 (1999)
33. O.M. Hemeda, M.A. Barakat, J. Magn. Magn. Mater. **323**, 127 (2001)
34. B.J. Evans, L.-S. Pan, J. Appl. Phys. **61**, 4352 (1987)
35. V.I. Nikolaev, V.S. Rusakov, N.I. Chistyakova, Phys. Lett. A **99**, 253 (1983)
36. R.E. Vandenberghe, E. De Grave, *Mossbauer spectroscopy applied to inorganic chemistry*, edited by G. Jdong, F. Grandjean (Plenum Press, New York, 1988), Vol. 3, p. 143